Original Article

D. G. K. Kalara Namawardana, R. M. Geethanjana Wanigasekara, W. T. M. Aruna P. K. Wanninayake, K. M. D. Charith Jayathilaka, Ruwan P. Wijesundera*, Withana Siripala and Muhammad Imran Malik

Fabrication of inverted organic solar cells on stainless steel substrate with electrodeposited and spin coated ZnO buffer layers

https://doi.org/10.1515/polyeng-2021-0280
Received September 24, 2021; accepted November 26, 2021; published online January 13, 2022

Abstract: Polymer based organic solar cells (OSCs) are of tremendous interest as suitable candidates for producing clean and renewable energy in recent years. In this study, inverted OSCs on stainless steel (SS) substrate with zinc oxide (ZnO) as the electron selective transport layer (ESTL), are investigated, occupying bulk heterojunction blend of regioregular poly(3-hexylthiophene) (P3HT) and phenyl-C61-butyric acid methyl ester (PCBM) as the active material and poly-(4,3-ethylene dioxythiophene):poly(styrenesulfonate) (PEDOT:PSS) as the hole transport layer (HTL). The device structure is SS/ZnO/P3HT:PCBM/PEDOT:PSS/Au. ZnO films are prepared by spin coating and electrodeposition techniques, followed by annealing under ambient conditions. The insertion of ZnO layer between the SS substrate and active layer has improved short-circuit current (J_{sc}), open-circuit voltage (V_{oc}), fill factor (FF), and power conversion efficiency (PCE) compared to those of the reference cell without ZnO layer, achieving the highest efficiency of 0.66% for the device with spin coated ZnO from sol–gel technique. This enhancement can be attributed to the effective electron extraction and the increased crystallinity of ZnO after annealing treatments at higher temperatures as further confirmed by X-ray diffraction (XRD) and scanning electron microscope (SEM) analyses.

Keywords: electrodeposition; inverted organic solar cells; P3HT: PCBM; spin coating; zinc oxide.

***Corresponding author: Ruwan P. Wijesundera,** Department of Physics and Electronics, University of Kelaniya, Dalugama Kelaniya 11300, Sri Lanka, E-mail: palitha@kln.ac.lk. https://orcid.org/0000-0002-3223-5969
D. G. K. Kalara Namawardana, R. M. Geethanjana Wanigasekara, W. T. M. Aruna P. K. Wanninayake, K. M. D. Charith Jayathilaka and Withana Siripala, Department of Physics and Electronics, University of Kelaniya, Dalugama Kelaniya 11300, Sri Lanka
Muhammad Imran Malik, Third World Center for Science and Technology, H.E.J. Research Institute of Chemistry, International Center for Chemical and Biological Sciences (ICCBS), University of Karachi, Karachi 75270, Pakistan

1 Introduction

In recent years, organic solar cells (OSCs) have received more academic and industrial attention over the conventional inorganic counterparts, owing to its low cost, lightweight, high mechanical flexibility and large-area processability with significant progress in power conversion efficiency above 18% [1–4]. Out of organic solar cells, bulk heterojunction organic solar cells (BHJ-OSC) based on regioregular poly(3-hexylthiophene) (rr-P3HT) as donor and [6,6]-phenyl-C61-butyric acid methyl ester (PCBM) as acceptor, have been widely investigated, achieving best certified efficiency of 5.4% [5, 6]. Although most of the fabrications of P3HT:PCBM based OSCs have been reported conducting on indium-tin oxide (ITO) coated glass substrates using conventional structure, active layer is more prone to oxidation and degradation due to the diffusion of oxygen and moisture through air-sensitive low-work-function metal cathodes such as Al in this structure [7]. Hence, recent research attention has been shifted on utilizing the inverted structure for fabrications as it allows using less air sensitive and more stable high work function metals (Ag, Au) as the top electrode [8].

Furthermore, ITO glass substrates could not fulfill the requirements of large scale fabrication due to its rigid nature, intrinsic brittleness and high production cost as Indium is a scarce and expensive element [9]. These limitations of ITO have been motivating the search for novel materials suitable for low cost and flexible OSCs, such as novel metal oxides, conducting polymers, carbon nanomaterials, metal nanowires, metal films and metal meshes

[10–15]. Among those materials, stainless steel (SS) metal substrates possess many distinct qualities of cost-effectiveness, high strength, compatibility with roll-to-roll processing, excellent dimensional and thermal stability at high processing temperatures, good resistance to chemicals, and a strong barrier to water vapor and oxygen [16, 17]. Another key benefit of OSCs fabricated on SS substrates is, they can be incorporated with roof surfaces since low-carbon steel is mostly used as a rooftop material for buildings, making the rooftop as an integrated power source [18]. However, one of the few challenges SS substrate brings, is the necessity of top illumination due to its opaqueness. Hence, the top electrode of inverted OSCs must be semi-transparent for sufficient amount of light to reach the active layer. Few earlier studies have utilized semitransparent ultrathin films of Au and Ag as top contacts [19, 20].

Although solar cell devices on SS substrates have been thoroughly researched through years, there are only a few studies available, of BHJ-OSCs fabricated on SS substrates [21, 22]. Galagan et al. has reported P3HT:PCBM based OSCs fabricated on SS substrates in conventional structure with efficiency of 1.30%, whereas Chang et al. has reported 0.97% efficiency with inverted OSCs [17, 23]. Efficiencies of 2.1 and 3.1% have been achieved by Gupta et al. for P3HT:PCBM layers fabricated on insulated steel substrates in inverted and conventional structure respectively [24]. Inverted OSCs fabricated on insulated low-carbon steel substrates by Pali et al. has reached a PCE of 1.35% [18]. The latter studies have not used the conductive properties of the substrate by completely insulating it from the actual OSC device with an insulating planarization layer in order to minimize the substrate roughness [18, 24]. However this insulation limits the utilization of SS as a back contact with low sheet resistance (0.9 Ω/sq). Thus to minimize the surface roughness, a buffer layer can be embedded between the SS substrate and active layer instead of an insulation layer.

This buffer layer also can act as an electron selective transport layer (ESTL) to improve the efficiency of inverted OSCs [25]. In recent studies, thin metal oxide films of titanium oxide (TiO_2, TiO_x) and zinc oxide (ZnO) have been mostly used as potential candidates for ESTL [19, 26]. Compared with titanium oxide, ZnO possess many advantages including high electron mobility, direct wide band gap (3.37 eV), environmental stability, and low cost, making it the most widely used buffer layer in inverted OSCs [27, 28]. ZnO ESTL can reduce charge recombinations and increase charge transfer efficiency, improving the efficiency of the device due to its proper energy level alignment with PCBM acceptors in collecting electrons and blocking holes effectively from P3HT. Thin films of ZnO can be deposited by several chemical methods such as chemical bath deposition (CBD), electrodeposition, sol-gel synthesis, hydrothermal synthesis, spray pyrolysis etc. [29–33]. Among them sol–gel technique has been widely used as a simple, low cost and large area deposition technique [34]. Conversely, electrodeposition is scarcely investigated as a technique to synthesize ZnO buffer layers of inverted OSCs, even though it shows many advantages such as simplicity, low cost, self-purification capability, and ability to produce high quality-material layers [35]. In this study we fabricate inverted P3HT:PCBM based OSC devices on SS substrate with ZnO buffer layers using electrodeposition and sol–gel spin coating techniques and analyze the effect of ZnO layers upon the device performance. We further analyze the device stability under ambient conditions.

2 Materials and methods

2.1 Materials

P3HT (>99%) was purchased from Sigma Aldrich, USA. PCBM (>99%) was purchased from Sigma Aldrich, Netherlands. Mono-chlorobenzene (MCB) (>99.5%) was purchased from Sigma Aldrich, Germany. PEDOT:PSS (1.3 wt.%, conductive grade) was purchased from Sigma Aldrich, USA. 304 Grade SS sheets were purchased from Sri Lanka. Zinc acetate dihydrate ($Zn(CH_3CO_2)_2{\cdot}2H_2O$) (>99.5) was purchased from FreyaLab, Bulgaria. Zinc nitrate hexahydrate ($Zn(NO_3)_2{\cdot}6H_2O$) (≥99.0%) was purchased from Sigma Aldrich, Croatia. Methanol (>99.8%) was purchased from Sigma Aldrich, USA.

2.2 Fabrication of devices

In electrodeposition technique, thin films of ZnO were electrodeposited on SS substrates (area ~2 × 2.5 cm^2) in an aqueous solution containing 0.025 M zinc nitrate. The temperature of the electrolyte was maintained at 60 °C and counter and reference electrodes were a platinum plate and a saturated calomel electrode (SCE), respectively. The electrodeposition was carried out under a potentiostatic condition of –975 mV versus Ag/AgCl for 10 min using Potentiostat/Galvanostat (Hokuto Denko HAB 151). During the electrodeposition, the baths were continuously stirred using a magnetic stirrer. After growth of the films by the electrodeposition technique, they were placed in a furnace and annealed at 500 °C for 60 min in air.

In spin coating technique, a solution containing 0.5 M zinc acetate dihydrate was prepared in methanol and magnetically stirred for 30 min at the room temperature. The solution was aged 24 h before the coating. Aged solution was spin coated on SS substrates (area ~2 × 2.5 cm^2) at 4000 rev./min for 30 s and subsequently the film was annealed at 250 °C for 10 min in air. This procedure was repeated several times to obtain a thin film of desired thickness. Finally, the whole stack was annealed at 500 °C for 60 min in air. Prior to the growth of ZnO in both processes, polished SS substrates were ultrasonically cleaned stepwise in detergent, DI water, acetone, methanol and 2-propanol and subsequently dried in air.

Bulk-heterojunction polymer blend was prepared by mixing regioregular P3HT and PCBM with a weight ratio of 1:1 in MCB (20 mgmL^{-1}) and stirred at 55 °C for 12 h. Then this blend was spin coated on pre-cleaned SS substrates or ZnO layers and later annealed at 120 °C for 30 min to form the active layer. Conductive grade, 1.3 wt.% dispersion of PEDOT:PSS in H_2O was doped with ethylene glycol (EG) to prepare a 10 wt.% solution and stirred at room temperature for 12 h. It was blade-coated on the active layer and the stack was annealed at 120 °C for 10 min. Finally, as the top contact of the device, gold (Au) spots were sputter coated. The cross sectional view of the final device structures with and without ZnO is schematically shown in Figure 1. The device performance was optimized by varying the spin speed of the active layer formation, annealing conditions (temperature and duration) of the active layer and dopant material of PEDOT:PSS solution.

2.3 Device characterization

The devices were top illuminated under 1 sun illumination (AM 1.5G, 1000 Wm^{-2}) of Sciencetech Scisun-300 solar simulator and dark and light J-V characteristics were measured using Gamry series G300 potentiostat/Galvanostat. Open circuit voltage (V_{oc}), short circuit current density (J_{sc}), power conversion efficiency (PCE), and fill factor (FF) of fabricated devices were obtained using J-V characteristics of the devices. Spectral responses of the cells were measured using a computer controlled system consisting of Stanford Research-SR 830 DSP lock-in amplifier, ScienceTech 9010 (200–1200 nm) monochromator and a Standford Research-SR 540 chopper. The crystallinity of the produced films was studied by using Bruker D8 Advance ECO X-ray diffractometer with wavelength of 1.54 Å (Cu K_α radiation). Surface topographical analysis was conducted by using Hitachi SU6600 Scanning Electron Microscope.

3 Results and discussion

In this study, inverted OSCs were fabricated on SS substrates with and without ZnO thin films to compare their device performances. Two methods, Spin coating and electrodeposition, were employed to grow ZnO layers to study the effects of growth techniques and annealing effect of deposited ZnO layers on the device performance. All other parameters including, the chemical composition and microstructures, were controlled to be the same. Fabricated devices were top illuminated through semi-transparent Au spots (area ~2 × 2 mm^2) with thickness of ~20 nm. The active area exposed to light was 1 × 1.5 cm^2. The J-V curves of those devices are shown in Figure 2 and the best performance parameters, including V_{oc}, J_{sc}, FF, and PCE are listed in Table 1.

The reference device which was fabricated on SS substrate itself without ZnO layer exhibited maximum PCE of 0.24% with J_{sc} at 4.36 mAcm^{-2} and FF at 23.19%. However, there is only a slight photovoltaic response produced by the device with spin coated and non-annealed ZnO layer as J_{sc} of 0.04 mAcm^{-2} and V_{oc} of 81.7 mV compared with other devices fabricated incorporating a ZnO layer. This can be attributed to the non-crystalline structure of the ZnO formed. Most of the previous reports on solution-cast ZnO buffer layers have mentioned that an annealing temperature above 300 °C is required to realize crystalline ZnO films with high carrier mobility in order to improve OSC efficiency [36]. Therefore, it implies that non-annealed condition has produced an amorphous ZnO buffer layer with the poor crystallinity which results low conductivity ZnO film yielding poor device performance. This can be further confirmed by X-ray diffraction (XRD) patterns which will be presented later. Further it can be seen that incorporating a ZnO ESTL between SS substrate and P3HT:PCBM active layer and subsequent annealing at 500 °C for 60 min, have increased J_{sc}, $V_{oc,}$ FF and PCE significantly. For the device with spin coated and annealed ZnO layer, J_{sc} increased from 4.36 to 6.21 mAcm^{-2} and the FF increased from 23.19 to 31.09% while V_{oc} increased from 238.1 to 344.2 mV. As a result, highest PCE among this set was 0.66%. Considering the fact that higher response can be obtained after

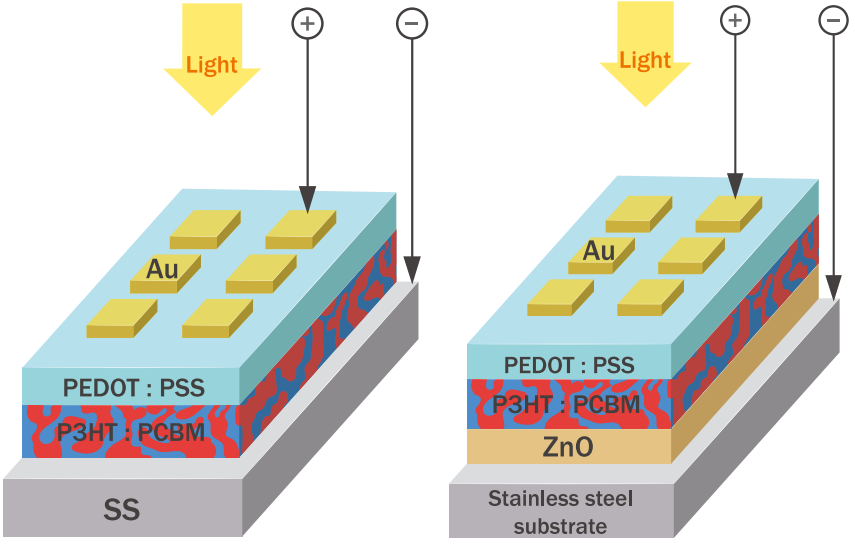

Figure 1: Schematic diagram of cross section of top illuminated inverted OSCs on SS substrates (a) without and (b) with ZnO buffer layer.

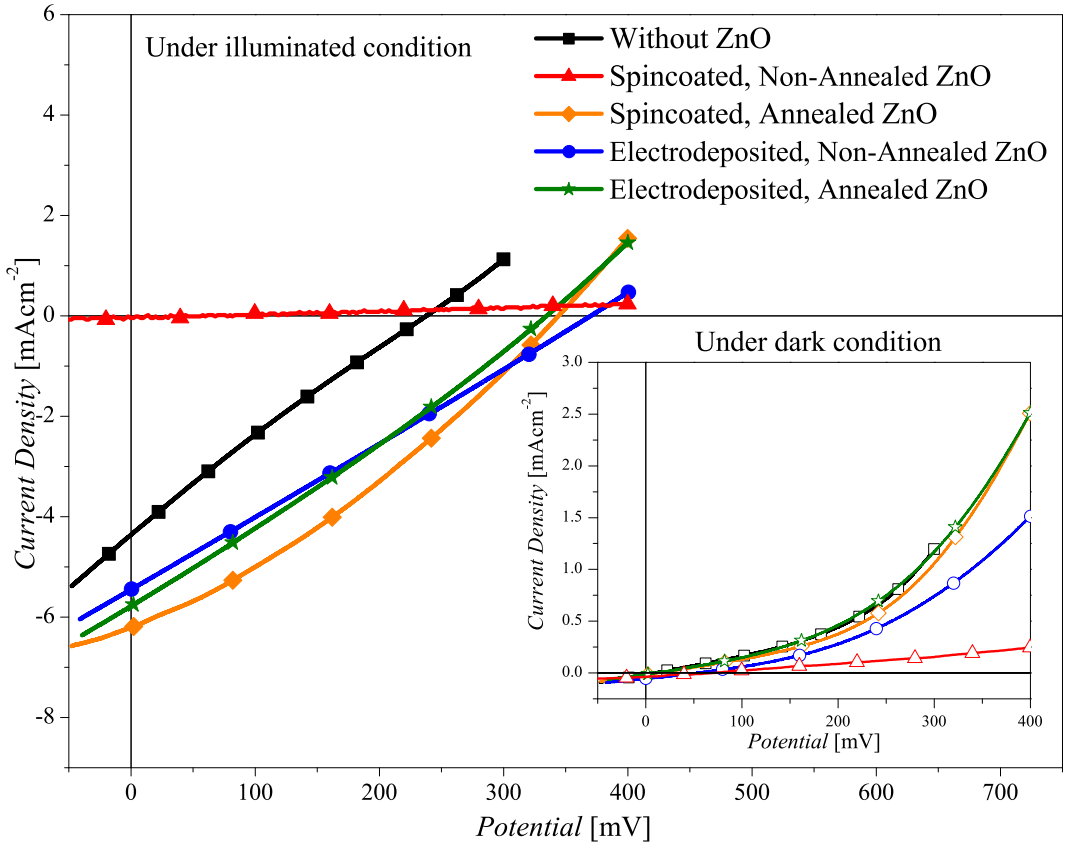

Figure 2: Dark and light J-V curves of the fabricated devices.

Table 1: Best photovoltaic parameters of fabricated OSCs.

Fabricated device	J_{sc} (mAcm^{-2})	V_{oc} (mV)	FF %	PCE %
Samples without ZnO layer	4.36	238.1	23.19	0.24
Samples with spin coated and non-annealed ZnO layer	0.04	81.7	0.00	0.00
Samples with spin coated and annealed ZnO layer	6.21	344.2	31.09	0.66
Samples with electrodeposited and non-annealed ZnO layer	5.45	370.1	25.46	0.51
Samples with electrodeposited and annealed ZnO layer	5.78	334.7	27.12	0.52

annealing of spin coated ZnO buffer layer, the annealing step which yields a crystalline state of ZnO has played a crucial role in improving device performances. Comparatively, the devices with electrodeposited ZnO ESTL also show a significant enhancement in device performance characteristics. The J_{sc} has increased from 4.36 to 5.45 mAcm^{-2} after electrodepositing the ZnO layer and it was further increased to 5.78 mAcm^{-2} by annealing the ZnO layer. The FF also follows the similar trend and it has improved from 23.19 to 25.46% and further improved to 27.12% after thermal annealing. This results clearly indicate that ZnO ESTL and annealing treatment enhance the device performance with compared to the device without a ZnO ESTL, due to the fact that the crystalline state of ZnO is believed to promote efficient electron transfer through the film.

In order to assess the effect of ZnO layer on the improvement of device performances, shunt resistance (R_{sh}) and series resistance (R_s) of fabricated devices were calculated from J-V curves as listed in Table 2. R_{sh} is what determine the leakage current by providing an alternate current path for the photo-generated current, whereas R_s is resulting from the composed layers of fabricated device [37]. As listed in Table 2, the device without ZnO shows comparatively higher R_s which leads to lower J_{sc} value and lowered R_{sh} yielding poor FF ultimately resulting in a lower PCE. This decline can be mainly attributed to the poor charge transfer across the device resulting in higher charge carrier recombinations. However, when ZnO layer is incorporated, R_s has seemingly decreased and R_{sh} has increased in both devices with spin coated and electrodeposited ZnO layers leading to higher J_{sc}, FF, and PCE. This confirms that ZnO layer assists efficient charge transfer, working as an effective ESTL minimizing the charge recombinations. ZnO has

Table 2: Shunt resistance (R_{sh}) and series resistance (R_s) of fabricated OSCs.

Fabricated device	R_s (Ω cm^2)	R_{sh} (Ω cm^2)
Without ZnO layer	61.12	48.57
With spin coated and annealed ZnO	37.63	112.12
With electrodeposited and annealed ZnO	47.50	66.93

further enhanced the exciton dissociation at the active layer and ZnO interface and increased the number of excitons between acceptor and donor materials improving the V_{oc} of the devices.

Spectral response curves of the fabricated devices are shown in Figure 3. It is clear that, all of these devices, with and without ZnO ESTL have shown responses in the visible wavelengths of the electromagnetic spectrum. Photon absorption of the devices with ZnO films closely resemble with each other; however excess photon absorption can be clearly seen in the short wavelength region of 450–500 nm with spin coated ZnO layer. In contrast, device without ZnO and with electrodeposited ZnO layers tend to absorb more photons in the range of 500–550 nm. In the short wavelength range, device with spin coated ZnO ESTL, gives a flattened curve rather than the bell-shaped curve of the device without ESTL. All the devices showed a band edge range between the 660 and 675 nm level indicating a band gap energy range between 1.87 and 1.84 eV. Lower energy photons are not absorbed due to the higher energy level differences in the HOMO and LUMO levels of the P3HT. Once the threshold energy 1.84 eV is achieved, the photons

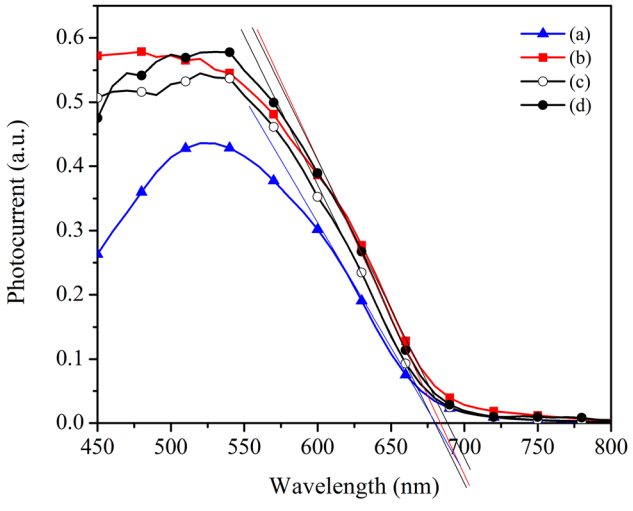

Figure 3: Spectral response curves of fabricated devices: (a) Without ZnO, (b) With spin coated and annealed ZnO, (c) With electrodeposited and non-annealed ZnO, (d) With electrodeposited and annealed ZnO.

are absorbed causing a photocurrent. However, the higher energy photons transmit through the active material without absorptions. This decrease in absorption causes lower photo-response in the higher energy region.

Figure 4 shows XRD patterns of SS substrate and as-deposited and annealed ZnO thin films grown by spin coating and electrodeposition techniques. Diffraction patterns of SS substrates shows that the crystal structure of these samples consists of austenite phase with peak planes (111), (200) and (220) [38]. All the diffraction patterns of deposited ZnO thin films except the pattern of spin coated and non-annealed ZnO indicate that they are polycrystalline in nature having hexagonal wurtzite structure with prominent three diffraction peaks for the planes (100), (002) and (101). XRD pattern of spin coated and annealed ZnO layer shows a well-defined crystalized structure with diffraction peaks (100), (002), (101), (102), (110), (103), and (112) [39]. This improvement of crystallinity can be ascribed to the best device performance out of all the devices with higher electron mobility through the ZnO ESTL. On the contrary, there are no distinct peaks of hexagonal wurtzite structure present in spin coated and non-annealed ZnO layer, since the material is amorphous before annealing. This poor crystallinity and an amorphous structure further explain the poor device performances. However, diffraction patterns of as-deposited and annealed ZnO films deposited via electrodeposition technique show somewhat similar crystal structure with dominant peaks representing the planes (002) and (101). The most intense peak of XRD patterns was along the (002) plane on the contrary to spin coated and annealed ZnO film. Further it can be noticed that in both patterns, (100) plane is not significantly formed. Annealing of electrodeposited ZnO thin film has increased the intensity of peaks (002) and (101) indicating the crystallinity of the film has been improved. This can be considered as the reason for the slight enhancement of device characteristics between devices as-deposited and annealed ZnO ESTL. Figure 5 shows the XRD patterns of SS/P3HT:PCBM and SS/ZnO/P3HT:PCBM devices. In both spectrums, in addition to the peaks assigned for SS and ZnO, a broad peak around 5.37 2θ degree is observed due to the reflection plane (100) of thiophene rings in P3HT chain. P3HT:PCBM blend is originally amorphous, however P3HT has the ability to crystalline upon annealing at elevated temperatures [40].

Figure 6a shows scanning electron microscopic (SEM) images of the surface morphology of spin coated ZnO films prepared by annealing at 500 °C for 60 min. According to the image, film exhibits a granular surface morphology with a grain size of about 500 nm. As depicted in Figure 6b SEM micrograph of electrodeposited and annealed at

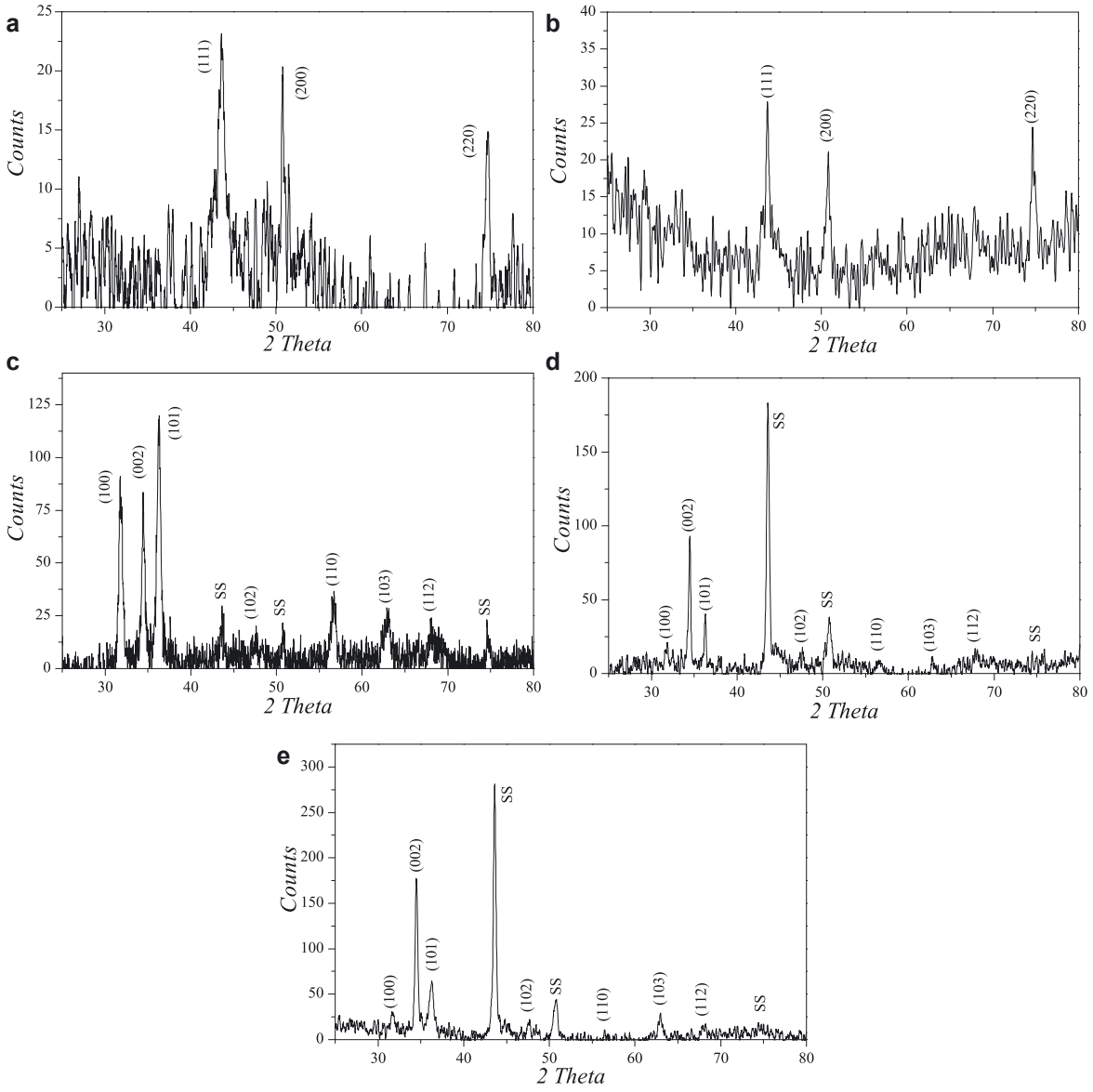

Figure 4: XRD patterns of (a) SS substrate, (b) spin coated and non-annealed ZnO on SS substrate, (c) spin coated and annealed ZnO on SS substrate, (d) electrodeposited and non-annealed ZnO on SS substrate and (e) electrodeposited and annealed ZnO on SS substrate.

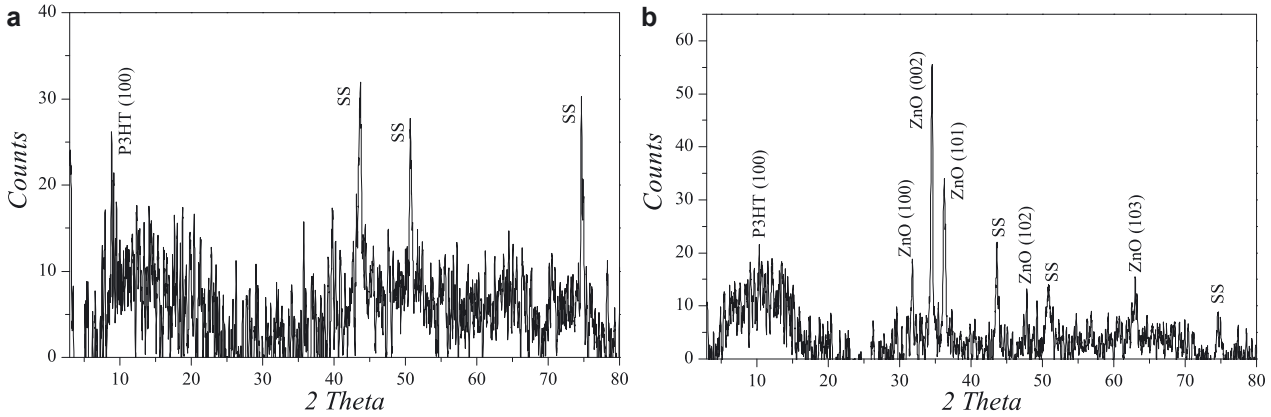

Figure 5: XRD patterns of (a) SS/P3HT:PCBM and (b) SS/ZnO/P3HT:PCBM.

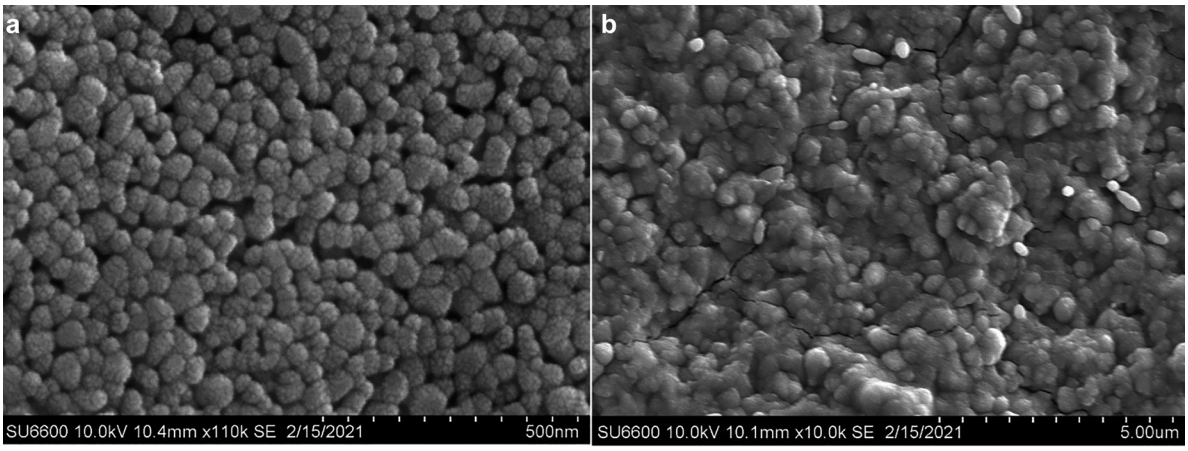

Figure 6: SEM images of (a) spin coated and annealed at 500 °C ZnO thin film and (b) electrodeposited and annealed at 500 °C ZnO thin film.

500 °C for 60 min ZnO thin film shows the polycrystalline ZnO films to have a granular structure with average grain size of about 3–5 μm. Comparatively, the grain size of ZnO thin film deposited by spin coating is smaller than that of electrodeposited ZnO film. The grain size affects the surface roughness which plays an important role on the device performance by altering the effective interfacial area between the ZnO layer and the active layer. Larger grain size of electrodeposited ZnO thin film leads to an increase in surface roughness resulting larger contact area at interface which can produce more interface traps and further increase contact resistance [41]. These interface traps allow charge accumulation and undesired trap-assisted recombinations at the surface, preventing efficient charge transport from the active layer to ZnO layer. Thus, this increment of charge recombinations and contact resistance could be attributed to the lower values of J_{sc}, FF, and PCE of the device fabricated with electrodeposited ZnO. Even though this ZnO film is densely packed, visible cracks on the surface have also caused negatively on the device performances due to the degraded quality of the film's physical properties. Conversely, ZnO thin film synthesized via sol-gel spin coating process shows more uniform film surface with smaller sized grains and minimal surface roughness which facilitates an efficient charge transfer at the surface, resulting in better device performance. However, it shows some nano-voids and nanopores in the film, which negatively effect on the charge transfer through the ZnO layer.

Although the efficiency of the devices with ZnO ESTL has more than twice improved of that of the device without ZnO, resulted values of device parameters are smaller than the state of art efficiencies with the similar device architecture. This insufficient device performance can be ascribed to several causes. In preparation of ZnO ESTL, annealing at higher temperature is essential to achieve high crystallinity and high conductivity of the ZnO film. Unfortunately, high thermal treatments give rise to the surface roughness of the ZnO film which reduces R_{sh} of the cell leading to a higher leakage current and poor device characteristics [42]. Moreover, manufacturing defects during the fabrication process also cause significant power losses. In this study, HTL of EG/PEDOT:PSS was manually blade coated by smearing it over the active layer with the help of a glass slide due to its poor wettability and inability to spin coat on hydrophobic P3HT:PCBM layer. However, there could be some variation in the film thickness resulted across the film; hence different drying dynamics could alter the orientation of PEDOT grains within the film. This could lead to changes in conductivity and surface properties of PEDOT:PSS lowering the device performances [43].

A degradation study of the devices with and without ZnO ESTL was carried out through a time span of 50 days under shelf-life conditions in air atmosphere. The devices were sandwiched between transparent acrylic sheets. Figure 7 graphically shows the change of short circuit current density (J_{sc}), open circuit voltage (V_{oc}), bulk resistance of the device (R), FF and PCE during the time period. J_{sc}, FF and PCE of the devices show a sudden drop in the device performance at the beginning of the device operation, which is called 'burn-in' loss, due to a non-recoverable permanent degradation. After that device characteristics follow a linear decay until it reaches a steady level. When consider J_{sc}, it can be observed that current density has gradually decreased with time in all three devices. In the device fabricated without ZnO, the change is more rapid than the other two devices fabricated with ZnO layer and it has decreased by 80.6% compared to its initial value. However, in the devices with electrodeposited ZnO and spin coated ZnO, the changes are

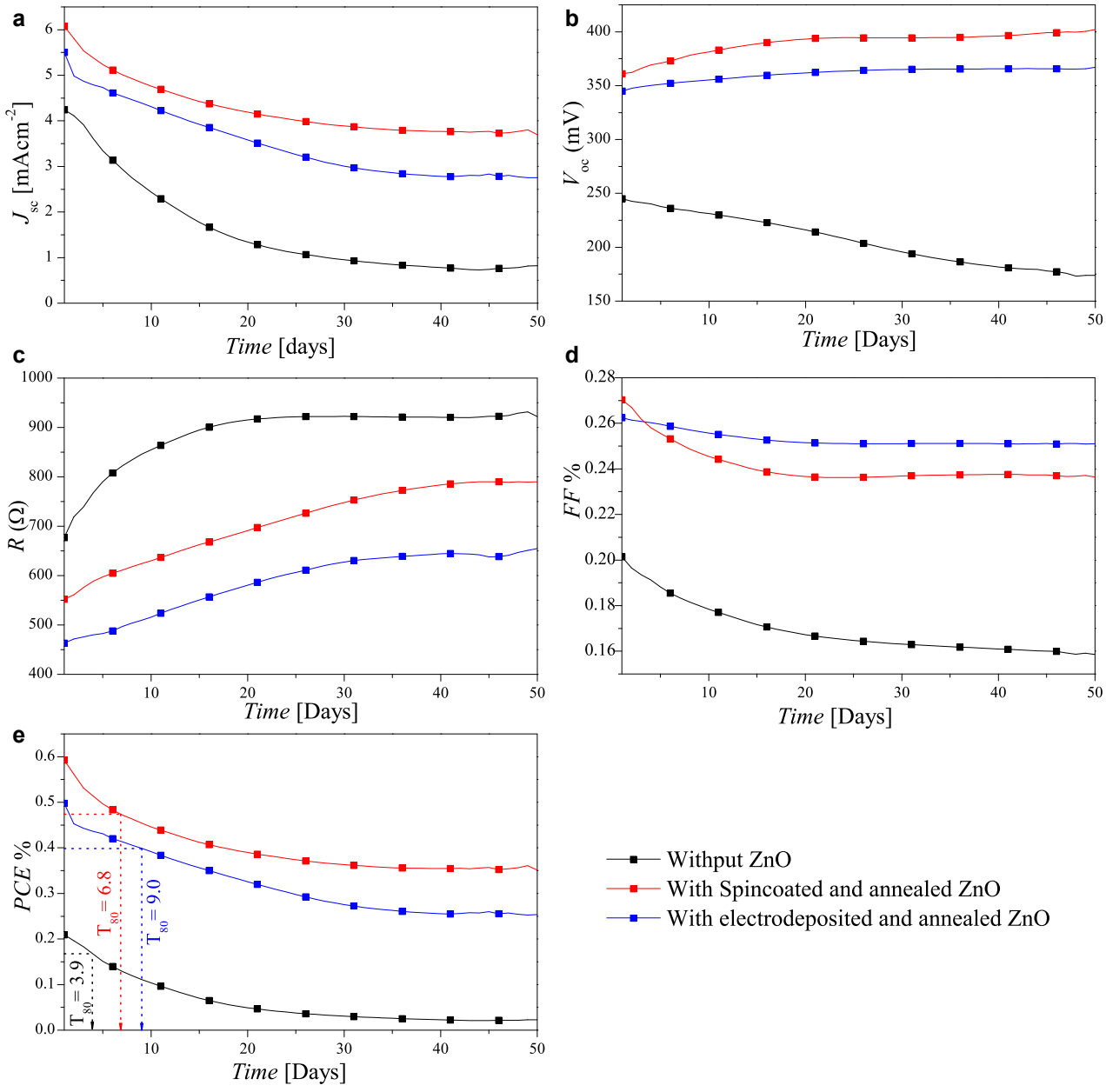

Figure 7: Change of (a) J_{sc}, (b) V_{oc}, (c) R, (d) FF and (e) PCE during 50 day time span.

by 49.9 and 39.1% respectively. During the last 10 days, all three devices have reached to a steady level. Considering open circuit voltage of the fabricated devices, V_{oc} has slightly increased in the devices with ZnO ESTL whereas a reduction is observed in the device without ZnO. In the devices with ZnO it has reached to a steady level during last 10 days, while it continues to decrease in the absence of ZnO layer. R has gradually increased in all three devices with a higher resistance and a rapid growth was resulted for the device without ZnO. Moreover, there is a depletion of FF in all three devices caused by increasing R. The change of power conversion efficiency follows a similar way of reduction to J_{sc} change, given the fact that PCE is directly based on J_{sc}. PCE of the device without ZnO have decreased significantly compared to other two devices. The device stability can be evaluated by calculating T_{80} value which is defined as the time it takes for the PCE to decay to 80% of its initial value. The device without ZnO shows a T_{80} of 3.9 days while devices with spin coated and electrodeposited ZnO present 6.8 and 9.0 days, respectively. Out of the two methods used for the fabrication of ZnO film, device with electrodeposited ZnO seems to be more stable with higher T_{80}, despite its low J_{sc}, FF and PCE compared to the device with spin coated ZnO.

The degradation of OSCs is caused by a wide range of phenomena occurring simultaneously of which many are scarcely investigated yet. When OSC devices are exposed to light, degradation can occur in photoactive layer due to photochemical damages or by the elevated temperatures, changing the properties of the active layer. Even though the devices were encapsulated between acrylic sheets, water and oxygen molecules can ingress through the edges and cause photo-oxidation of the active layer and interfaces, which consequently will alter its absorption, energy levels and charge carrier mobilities [44, 45]. These factors considerably affect the excitons generation, reducing J_{sc}, FF and PCE of the device. Also due to the hygroscopic PSS in PEDOT:PSS, colloidal particles in the dispersion swell considerably by absorbing moisture and form a closed surface layer, increasing the series resistance with reduced conductivity. The degradation is more prominent in the device without ZnO layer with lower T_{80} value compared with other two devices with ZnO. It can be attributed to that ZnO ESTL has contributed to reduce the bulk resistance and increase the device stability in the devices with ZnO. However, the reactivity of ZnO with air and light, can cause charge carrier trapping and recombinations at the interface, eventually reducing the J_{sc} and FF as well as the device lifetime of the cells with ZnO layers [46].

4 Conclusions

In this study inverted P3HT:PCBM organic solar cells were fabricated on SS substrates with and without ZnO ESTL via two different techniques, spin coating and electrodeposition. The results indicate that incorporating an ESTL between SS substrate and active material has significantly increased the device characteristics including J_{sc}, V_{oc}, FF and PCE by reducing charger recombinations and increasing charge transfer efficiency. The highest efficiency of 0.66% was resulted by the device with spin coated ZnO layer. The highly crystalized structure of ZnO indicated by XRD pattern and uniform and smaller grain size further confirms the improved device performances. It can be further noticed that subsequent annealing of deposited ZnO film at 500 °C for 60 min has enhanced the device performance of spin coated ZnO. Annealing at higher temperatures changes the amorphous nature of the film into a higher degree of crystallinity as confirmed by XRD analysis. Furthermore, the spectral response by each device indicates that all these devices absorb photons in the visible region with absorption peaks present at the range of 450–600 nm. According to device stability measurements, out of the two methods used for the fabrication of ZnO film, device with electrodeposited ZnO is more stable with higher T_{80}, despite its low J_{sc}, FF, and PCE compared to the device with spin coated ZnO.

Author contributions: All the authors have accepted responsibility for the entire content of this submitted manuscript and approved submission.
Research funding: This work was financially supported by the National Science Foundation (NSF), Sri Lanka through research grant NSF-PSF/ICRP/2017EA&ICT/02.
Conflict of interest statement: The authors declare no conflicts of interest regarding this article.

References

1. Sun Y., Liu T., Kan Y., Gao K., Tang B., Li Y. Flexible organic solar cells: progress and challenges. *Small Sci.* 2021, *1*, 2100001.
2. Qin J., Lan L., Chen S., Huang F., Shi H., Chen W., Xia H., Sun K., Yang C. Recent progress in flexible and stretchable organic solar cells. *Adv. Funct. Mater.* 2020, *5*, 2002529.
3. Finn M., Martens C. J., Zaretski A. V., Roth B., Søndergaard R. R., Krebs F. C., Lipomi D. J. Mechanical stability of roll-to-roll printed solar cells under cyclic bending and torsion. *Sol. Energy Mater. Sol. Cells* 2018, *174*, 7–15.
4. Zhang M., Zhu L., Zhou G., Hao T., Qiu C., Zhao Z., Hu Q., Larson B. W., Zhu H., Ma Z., Tang Z. Single-layered organic photovoltaics with double cascading charge transport pathways: 18% efficiencies. *Nat. Commun.* 2021, *12*, 309–318.
5. Berger P. R., Kim M. Polymer solar cells: P3HT:PCBM and beyond. *J. Renew. Sustain. Energy* 2018, *10*, 013508.
6. Laird D. W., Vaidya S., Li S., Mathai M., Woodworth B., Sheina E., Williams S., Hammond T. Advances in Plexcore active layer technology systems for organic photovoltaics: roof-top and accelerated lifetime analysis of high performance organic photovoltaic cells. *Proc. SPIE 6656: Org. Photovoltaics VIII* 2007, 66560X; https://doi.org/10.1117/12.734711.
7. Abdallaoui M., Sengouga N., Chala A., Meftah A. F., Meftah A. M. Comparative study of conventional and inverted P3HT: PCBM organic solar cell. *Opt. Mater.* 2020, *105*, 109916.
8. Bowers N. M., Muller T. F. G., Arendse C. J., Oliphant C. J., Cummings F. R. Influence of the modification of annealing parameters on solution-processed metal oxide ETL buffer layers, and a comparative study of spin-coated and thermally evaporated MoOx HTL for use in an inverted polymer solar cell. *Mater. Today Proc.* 2021, *36*, 219–227.
9. Lu S., Sun Y., Ren K., Liu K., Wang Z., Qu S. Recent development in ITO-free flexible polymer solar cells. *Polymers* 2018, *10*, 5–34.
10. Hofmann A. I., Cloutet E., Hadziioannou G. Materials for transparent electrodes: from metal oxides to organic alternatives. *Adv. Electron. Mater.* 2018, *4*, 1700412.
11. Huseynova G., Kim Y. H., Lee J.-H., Lee J. Rising advancements in the application of PEDOT:PSS as a prosperous transparent and flexible electrode material for solution-processed organic electronics. *J. Inf. Disp.* 2020, *21*, 71–91.
12. Jeon I., Xiang R., Shawky A., Matsuo Y., Maruyama S. Single-walled carbon nanotubes in emerging solar cells: synthesis and electrode applications. *Adv. Energy Mater.* 2018, *9*, 1801312.

13. Dong X., Shi P., Sun L., Li J., Qin F., Xiong S., Liu T., Jianga X., Zhou Y. Flexible nonfullerene organic solar cells based on embedded silver nanowires with an efficiency up to 11.6%. *J. Mater. Chem. A* 2019, *7*, 1989–1995.
14. Bi Y.-G., Liu Y.-F., Zhang X.-L., Yin D., Wang W.-Q., Feng J., Sun H.-B. Ultrathin metal films as the transparent electrode in ITO-free organic optoelectronic Devices. *Adv. Opt. Mater.* 2019, *7*, 1800778.
15. Lee H. B., Jin W.-Y., Ovhal M. M., Kumar N., Kang J.-W. Flexible transparent conducting electrodes based on metal meshes for organic optoelectronic device applications: a review. *J. Mater. Chem. C* 2019, *7*, 1087–1110.
16. Kumar V., Wang H. Selection of metal substrates for completely solution-processed inverted organic photovoltaic devices. *Sol. Energy Mater. Sol. Cells* 2013, *113*, 179–185.
17. Galagan Y., Moet D. J. D., Hermes D. C., Blom P. W. M., Andriessen R. Large area ITO-free organic solar cells on steel substrate. *Org. Electron.* 2012, *13*, 3310–3314.
18. Pali L. S., Ganesan P., GargInverted A. P3HT PCBM organic solar cells on low carbon steel substrates. *Sol. Energy* 2016, *133*, 339–348.
19. Pali L. S., Gupta S. K., Garg A. Organic solar cells on Al electroded opaque substrates: assessing the need of ZnO as electron transport layer. *Sol. Energy* 2018, *160*, 396–403.
20. Patil B. R., Shanmugam S., Teunissen J.-P., Galagan Y. All-solution processed organic solar cells with top illumination. *Org. Electron.* 2015, *21*, 40–46.
21. Teraji S., Chantana J., Watanabe T., Minemoto T. Development of flexible Cd-free Cu(In,Ga)Se2 solar cell on stainless steel substrate through multi-layer precursor method. *J. Alloys Compd.* 2018, *756*, 111–116.
22. Sun K., Liu F., Huang J., Yan C., Song N., Sun H., Xue C., Zhang Y., Pu A., Shen Y., Stride J. A., Green M., Hao X. Flexible kesterite Cu_2ZnSnS_4 solar cells with sodium-doped molybdenum back contacts on stainless steel substrates. *Sol. Energy Mater. Sol. Cells* 2018, *182*, 14–20.
23. Chang Y.-M., Chen C.-P., Ding J.-M., Leu C.-Y., Lee M.-J., Chen R.-D. Top-illuminated organic solar cells fabricated by vacuum-free and all-solution processes. *Sol. Energy Mater. Sol. Cells* 2013, *109*, 91–96.
24. Gupta D., Wienk M. M., Janssen R. A. J. Efficient polymer solar cells on opaque substrates with a laminated PEDOT:PSS top electrode. *Adv. Energy Mater.* 2013, *3*, 782–787.
25. Zhang Q., Peng R., Zhang C., Chen D., Lin Z., Chang J., Zhang J., Hao Y. Inverted organic solar cells with low-temperature Al-doped-ZnO electron transport layer processed from aqueous solution. *Polymers* 2018, *10*, 127–139.
26. Al-Shekaili N., Hashim S., Muhammadsharif F. F., Al-Abri M. Z., Sulaiman K., Yahya M. Y., Ahmad M. R. Enhanced performance of PTB7:PC71BM based organic solar cells by incorporating a nano-layered electron transport of titanium oxide. *ECS J. Solid State Sci. Technol.* 2020, *9*, 105003.
27. Wei J., Zhang C., Ji G., Han Y., Ismail I., Li H., Luo Q., Yang J., Ma C.-Q. Roll-to-roll printed stable and thickness-independent ZnO:PEI composite electron transport layer for inverted organic solar cells. *Sol. Energy* 2019, *193*, 102–110.
28. Fei1 X., Jiang D., Wang N., Zhao H., Xing M., Li H. Study on ultraviolet photodetector modified by Au nanoparticles on ZnO nanowires. *J. Phys.: Conf. Ser.* 1907, *2021*, 012044.
29. Winkler N., Edinger S., Kautek W., Dimopoulos T. Mg-doped ZnO films prepared by chemical bath deposition. *J. Mater. Sci.* 2018, *53*, 5159–5171.
30. Rahal H., Kihal R., Affoune A. M., Ghers M., Djazi F. Electrodeposition and characterization of ZnO thin films using sodium thiosulfate as an additive for photovoltaic solar cells. *J. Semiconduct.* 2017, *38*, 053002.
31. Maroufa S., Beniaichea A., Guessasa H., Azizib A. Morphological, structural and optical properties of ZnO thin films deposited by dip coating method. *Mater. Res.* 2017, *20*, 88–95.
32. Muchuweni E., Sathiaraj T. S., Nyakotyo H. Effect of annealing on the microstructural, optical and electrical properties of ZnO nanowires by hydrothermal synthesis for transparent electrode fabrication. *Mater. Sci. Eng. B* 2018, *227*, 68–73.
33. Noh Y.-J., Na S.-I., Kim S.-S. Inverted polymer solar cells including ZnO electron transport layer fabricated by facile spray pyrolysis. *Sol. Energy Mater. Sol. Cells* 2013, *117*, 139–144.
34. Lin C.-C., Tsai S.-K., Chang M.-Y. Spontaneous growth by sol-gel process of low temperature ZnO as cathode buffer layer in flexible inverted organic solar cells. *Org. Electron.* 2017, *46*, 218–225.
35. Ojo A. A., Dharmadasa I. M. Electroplating of semiconductor materials for applications in large area electronics: a review. *Coatings* 2018, *8*, 262–278.
36. Arif M., Sanger A., Vilarinho P. M., Singh A. Effect of annealing temperature on structural and optical properties of sol-gel-derived ZnO thin films. *J. Electron. Mater.* 2018, *47*, 3678–3684.
37. Muhammad F. F., Sangawi A. W. K., Hashim S., Ghoshal S. K., Abdullah I. K. Simple and efficient estimation of photovoltaic cells and modules parameters using approximation and correction technique. *PLoS One* 2019, *14*, e0216201.
38. Quan C., He Y. Properties of nanocrystalline Cr coatings prepared by cathode plasma electrolytic deposition from trivalent chromium electrolyte. *Surf. Coating. Technol.* 2015, *269*, 319–323.
39. Post B., Weissmann S., McMurdie H. F., Eds. *Joint Committee on Powder Diffraction standards*. Inorganic Vol., Card No. 36-1451; Swarthmore, PA, 1990.
40. Munshi J., Dulal R., Chien T., Chen W., Balasubramanian G. Solution processing dependent bulk heterojunction nanomorphology of P3HT/PCBM thin films. *ACS Appl. Mater. Interfaces* 2019, *11*, 17056–17067.
41. Ma Z., Tang Z., Wang E., Andersson M. R., Inganäs O., Zhang F. Influences of surface roughness of ZnO electron transport layer on the photovoltaic performance of organic inverted solar cells. *J. Phys. Chem. C* 2012, *116*, 24462–24468.
42. Tsai J.-H., Tsai M.-C., Sung C.-Y., Huang P.-T. Significant increase in current density of inverted polymer solar cells by induced-crystallization of sol-gel ZnO embedded with ZnO-NP. *Org. Electron.* 2020, *86*, 105891.
43. Friedel B., Keivanidis P. E., Brenner T. J. K., Abrusci A., McNeill C. R., Friend R. H., Greenham N. C. Effects of layer thickness and annealing of PEDOT:PSS layers in organic photodetectors. *Macromolecules* 2009, *42*, 6741–6747.
44. Rafique S., Abdullah S. M., Sulaiman K., Iwamoto M. Fundamentals of bulk heterojunction organic solar cells: an overview of stability/degradation issues and strategies for improvement. *Renew. Sustain. Energy Rev.* 2018, *84*, 43–53.
45. Al-Shekaili N., Hashim S., Muhammadsharif F. F. Efficiency and stability improvement of organic solar cells based on PTB7: PCBM through hot-substrate coating. *J. Electron. Mater.* 2021, *50*, 6828–6835.
46. Cheng P., Zhan X. Stability of organic solar cells: challenges and strategies. *Chem. Soc. Rev.* 2016, *45*, 2544–2582.